A Digital Image-Based Method for Computational Tissue Fate Mapping During Early Avian Morphogenesis

EVAN A. ZAMIR,[1] ANDRÁS CZIRÓK,[1,2] BRENDA J. RONGISH,[1] and CHARLES D. LITTLE[1]

[1]The University of Kansas Medical Center, Department of Anatomy and Cell Biology, 3901 Rainbow Blvd, Kansas City, KS 66160; and
[2]Eötvös University Department of Biological Physics Pázmány Sétány 1/A Budapest, Hungary 1117

Abstract—The early stages of vertebrate development, encompassing gastrulation, segmentation, and caudal axis formation, presumably involve large (finite) morphogenetic deformations; however, there are few quantitative biomechanical data available for describing such large-scale or tissue-level deformations in the embryo. In this study, we present a new method for automated computational "tissue fate mapping," by combining a recently developed high-resolution time-lapse digital microscopy system for whole-avian embryo imaging with particle image velocimetry (PIV), a well-established digital image correlation technique for measuring continuum deformations. Tissue fate mapping, as opposed to classical cell fate mapping or other cell tracking methods, is used to track the spatiotemporal trajectories of arbitrary (virtual) tissue material points in various layers of the embryo, which can then be used to calculate finite morphogenetic deformation or strain maps. To illustrate the method, we present representative tissue fate and strain mapping data for normal early-stage quail embryos. These data demonstrate, to our knowledge, for the first time, large tissue-level deformations that are shared between different germ layers in the embryo, suggesting a more global morphogenetic patterning mechanism than had been previously appreciated.

Keywords—Biomechanics, Particle image velocimetry, Digital image correlation, Stress, Strain, Deformation, Notochord, Endoderm, Mesoderm, Fibrillin-2.

INTRODUCTION

During the early stages of embryonic morphogenesis, an extraordinarily dynamic process, significant tissue-level deformations and cell-level rearrangements continuously occur on time scales as brief as minutes. Local modulation of cell–extracellular matrix (ECM) and cell–cell interactions are required for a myriad of activities, such as cell-generated traction, motility, and shape-change—which finally result in the completion of a global embryonic plan or architecture.[5] The importance of physical forces in formation of the embryo cannot be overemphasized. Indeed,

in a recent review, Keller and colleagues[12] suggest that mechanical patterning connects the genetic, molecular, and cellular activities necessary for shaping the embryo at the macroscopic level. There are few experimental data addressing these inherently multi-scale phenomena in the embryo; therefore, it remains unclear how large-scale tissue design relates to cellular-level activities and biomechanical responses or feedback. In other words, how are microscopic processes integrated globally to produce the final embryonic form? This fundamental question remains open.

Classical cell fate mapping studies in many vertebrate species performed during the past century have documented the transition of progenitor cells into all major organ systems, and provided the framework for much of modern vertebrate developmental biology.[7] It is still not fully known, however, what contributions cells make to the determination of position-fate (i.e. pre-programmed), or to what extent cells may be carried or "convected" by global morphogenetic folding and convergent extension movements, in order to arrive at their definitive positions. Nor is it known by what means positional information is regulated.[6] It can be inferred from the results of cell fate mapping studies that cell displacement is due primarily to autonomous cell motility and migration. There are, however, at least four major concurrent large-scale morphogenetic deformations that could conceivably cause significant convective cell displacements during the later stages of gastrulation: (1) simultaneous notochord elongation and regression of the organizer (Hensen's node in birds); (2) neurulation or folding of the neural tube; (3) bilateral folding of the precardiac mesoderm to form the early heart tube; and (4) involution or folding of the primordial gut. Although it is presumably known that whole (epithelial) cell sheets can deform in the embryo, to our knowledge, the effects of such continuum deformations on cell fate mapping studies have not been studied, perhaps, because these types of macroscopic deformations have been more difficult to quantify *in vivo*. Therefore, the migration or motility of mesenchymal cells, such as neural crest and endothelial cells, may be superposed on (and masked by) larger-scale tissue motion,

Address correspondence to Charles D. Little, The University of Kansas Medical Center, Department of Anatomy and Cell Biology, 3901 Rainbow Blvd, Kansas City, KS 66160. Electronic mail: clittle@kumc.edu

involution, and folding. Separating these effects will not only enable more rigorous determination of cell motility *in vivo*, but will also help elucidate the nature and origin of biophysical forces driving these complex processes in the embryo.

Our lab has recently developed a multi-scale digital microscopy system for time-lapse imaging the entire avian embryo with cellular resolution.[3,22] We can now readily observe large-scale morphogenetic events in the embryo separated by distances on the order of 1 mm (e.g. heart development, segmentation, and notochord elongation) with spatial resolution approaching 1 μm. The avian embryo is ideal for these imaging studies, due to the following: (1) its relative robustness and ease of culture for a warm-blooded vertebrate embryo; (2) the essentially planar nature of the embryo; and (3) the ability to conveniently introduce experimental reagents. For example, by microinjecting fluorescently-labeled monoclonal antibodies into post-gastrulation stage quail embryos, we have analyzed the dynamic movements of a wide variety of tissue components, including the migration of endothelial cells (EC) during early vasculogenesis[20,21] and the dynamic motions of ECM fibrils during caudal axis formation.[2,5]

In this study, we introduce a new method for performing 'tissue fate mapping" in the embryo, wherein the trajectories of (arbitrarily placed) virtual material points in various tissue layers are automatically calculated using high-resolution (sub-pixel) digital particle image velocimetry (PIV) techniques, already well-established in other disciplines.[18,23] The derived tissue material displacement field is then naturally used to calculate regional morphogenetic strain maps. To illustrate the method, we present representative tissue-fate and strain-mapping data for normal early-stage quail embryos, which were cultured during the stages between primitive streak formation and heart looping. To our knowledge, these robust quantitative data are the first to demonstrate the development of large morphogenetic strains shared by multiple germ layers in the embryo.

METHODS

Quail Embryo Preparation

Quail embryos (*Coturnix coturnix japonica*, Ozark Egg Co., Stover, MO) were incubated at 37 °C in a humidified chamber to the desired Hamburger–Hamilton (HH) stages.[9] Embryos were then dissected from the egg and mounted on filter paper rings. During an experiment, embryos attached to paper rings were placed ventral-side up on larger plastic rings floating on liquid culture medium (Leibovitz-L15 supplemented with 2 mM L-glutamine, 10% chicken serum, and 1% penicillin–streptomycin) in a custom-built temperature—and humidity—controlled chamber mounted on the microscope stage. Details of the microscope culture chamber were given in a previous study.[3]

Fluorescent Labeling of Fibrillin-2

A monoclonal antibody to avian fibrillin-2,[19] JB3 (Developmental Studies Hybridoma Bank, University of Iowa), was directly conjugated to Alexa 647 (Molecular Probes), and microinjected into the lateral plate and caudal mesoderm (near Hensen's node) before the start of a time-lapse experiment. Microinjections were performed as previously described for whole-mount immunolabeling studies.[15]

Digital Time-Lapse Microscopy

The details of our digital time-lapse microscopy system have been fully described elsewhere.[3,22] Briefly, using custom-written software, a computer-controlled widefield (10X objective) epifluiorescent microscope (Leica DMR) workstation, equipped with motorized stage and cooled digital camera (Qlmaging Retiga 1300), is used to acquire 12-bit grayscale intensity images at multiple $x - y$ locations (fields) and focal planes (z-stacks). Automated switching of illumination modes and optical filters enables sequential acquisition of separate fluorescent wavelengths, in addition to brightfield or differential interference contrast (DIG) images. So, for one embryo, a single acquisition cycle or frame results in $n_f n_z n_i$ images, where n_f is the number of fields (usually 6–10), n_z is the number of focal planes (7–13), and n_i is the number of illumination modes. The exposure time, typically on the order of 100–500 ms, depends on both the robustness (i.e. brightness and stability) of the particular fluorochrome(s) used and the camera sensitivity. In general, frame rates range from 5–15 per hour in our setup. For a typical 10-h experiment, upwards of twenty-thousand images ($\sim$20 GB) are acquired. During an experiment, images are uploaded to a storage server (Xserv RAID, Apple, Inc.) for archiving and subsequent processing.

To reduce a 3-D tiled image data set to a single focused plane,[3] custom-written processing software automatically merges adjacent fields (i.e. mosaic-ing), and then collapses the merged focal planes using either a maximum local contrast algorithm or maximum through-plane grayscale intensity (i.e. z-projection), as is often done for confocal image sets. Typically, the local contrast method is used for brightfield or DIC images, and z-projection is used for fluorescent images. The resulting collapsed frames are then registered, using the center of the embryo as a reference location, thus correcting for any drift in the horizontal position of the embryo that may occur during an experiment, due to the nature of the ring culture method.[3]

Image-Based Tissue Fate Mapping

Preliminary Definitions

Let $I = I(t_i)$ be a single grayscale intensity image from a time-lapse experiment, where t_i is the *i*th time point ($i = 1 \ldots N$) and N is the total number of images in the sequence, so that a reference image $R = I(t_i)$ and any

arbitrary target image $T = I(t_{i+1})$ form an image-pair (R, T) to be analyzed by the correlation analysis described below. We assume that there exists a spatial mapping χ which transforms the grayscale intensities p according to $p(\mathbf{x}, T) = \chi(p(\mathbf{X}, R))$, where $\mathbf{X}$ and $\mathbf{x}$ are the image coordinates in the reference and target frames, respectively. For convenience, we define the first image in the time-lapse sequence $I_0 = I(t_1)$ to be the undeformed reference state or initial configuration for the tissue. Note that this choice is clearly arbitrary, and does not necessarily represent a stress-free state in the embryo, which in all likelihood, never truly exists. Let a 2-D region $\mathcal{R}$ of arbitrary shape and size in the initial configuration I_0 be defined by a set of virtual tissue material points or vertices $\mathcal{V}(x, y)$ to be fate mapped. The set of vertices was created automatically in any location of the embryo using a force-based method for producing high quality meshes with approximately uniform nodal spacing.[17] We note that the PIV method used here does not depend on any specific or pre-defined connectivity (i.e. edges) for the vertices, except for visualization purposes, as opposed to deformable block-matching image correlation algorithms. In practice, circular meshes are used for convenience and to enable more effective visualization of tissue deformation. Here, we will assume that the incremental displacement field for a single image pair (R, T) is given by $\mathbf{du} = \mathcal{V}(T) - \mathcal{V}(R)$. Likewise, for any current image I, the cumulative or total (material) displacement field in $\mathcal{R}$ is given by $\mathbf{u} = \mathcal{V}(I) - \mathcal{V}(I_0)$.

PIV Algorithm

The commercially-available mathematical programming language MATLAB (Mathworks, Inc., Natick, MA) was used to implement the following algorithm. Given an image pair (R, T), we desire a maximum-likelihood estimate (MLE) for the incremental displacement field $\mathbf{du}$. To determine $\mathbf{du}$, we used a two-step linear predictor–corrector approach, sometimes referred to as a window-offset method, which has essentially become a *de facto* PIV standard.[18,23] We note here that although PIV (and related digital image correlation) methods were first developed for measuring the motion of tracer particles in seeded flows, the theory can be applied generally to any sequence of images exhibiting correlated motion; therefore, PIV can be used to address problems in solid mechanics.[25] First, a coarse or predictor displacement field $\mathbf{du}^*$ for (R, T) was found using conventional normalized cross-correlation (normxcorr2 in MATLAB) operating on equally-spaced overlapping square blocks of pixels called sub-windows. Typically, the size s of the sub-window in R for this step was 128 pixels (square), and the maximum search radius r was 16 pixels (Fig. 1a). In
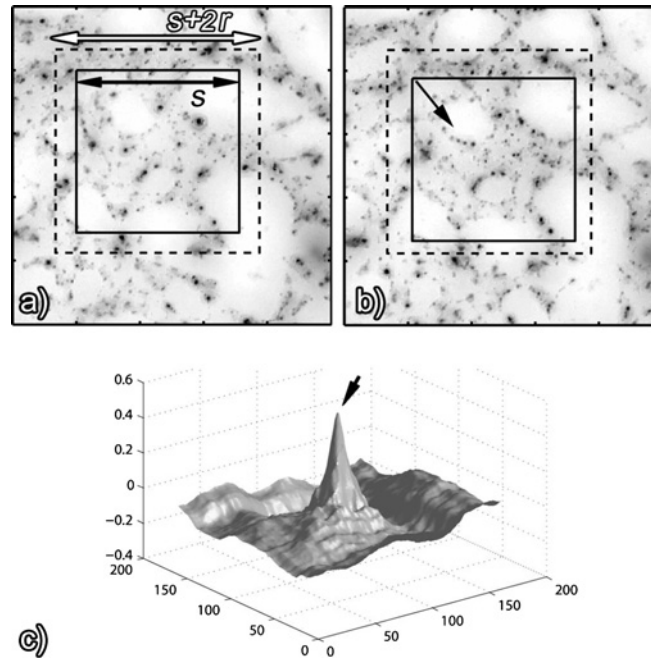

FIGURE 1. (a) Normalized cross-correlation is used to find the best match for a sub-window of width *s* (black double arrow) within a specified search area or interrogation window of width *s*+ 2*r* (white double arrow), thus providing the displacement vector (arrow) shown in (b). The location of the correlation function peak in (c) is found by three-point Gaussian interpolation (arrowhead). The images in (a) and (b) are from a time-lapse experiment in which the early vascular network was labeled using fluorescent-conjugated QH1 antibody, which is specific for quail endothelial cells. Note that although there is apparent variation in fine details between the two images, due primarily to cell movement, the change in the macroscopic pattern (i.e. tissue deformation) is almost imperceptible.
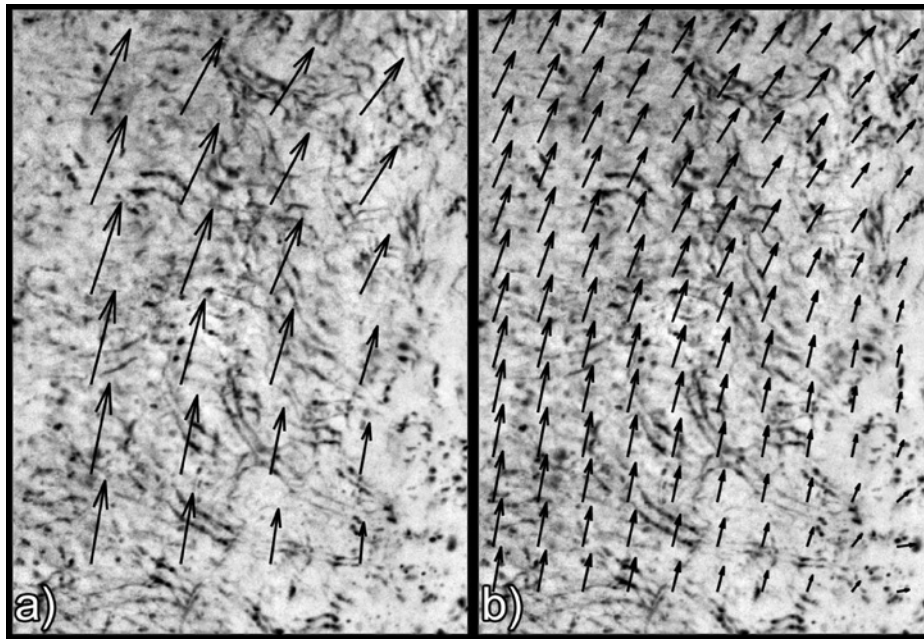
FIGURE 2. Double or summated images of fluorescent JB3-labeled fibrillin-2 in a small region of the embryo show local displacements of fibrils in a period of approximately 15 min. The physical displacements here are represented by the distance between pairs of identical parallel fibrils. Shown in (a) is a predictor or coarse displacement field approximation du* that was determined using 128-pixel blocks and 50% overlap (arrows indicate direction of displacement vectors). A corrector displacement field du** shown in (b) was calculated using 64-pixel blocks.

both the predictor step and subsequent corrector step, the sub-windows were typically overlapped by some amount (most often 50%) to improve both solution accuracy and smoothness. The displacement predictions (Fig. 2a) were then fitted by a thin-plate spline approximation (tpaps in the MATLAB Spline Toolbox), which served to simultaneously eliminate spurious displacement vectors and provide a continuous interpolating predictor function. It is essential to avoid false displacement vectors anywhere, because these can cause significant artifacts in the calculation of total material displacement and strain. We use the thin-plate spline approximation because it appears to offer the dual advantages of accuracy and smoothness.

In the corrector step, the (integer) displacement predictions were used to offset the sub-windows, and a search for the largest correlation peaks was repeated. In this step, however, the size of the sub-window was halved to $s = 64$ pixels, thus improving spatial resolution, while the search radius was typically reduced to $r = 4$ pixels, thereby reducing the number of spurious vectors. The values for the parameters r and s were chosen by trial-and-error to maximize spatial resolution and accuracy. We provide some discussion of these issues in the Results section. There are also many good references in the PIV literature on the topic of the window-offset method.[18,23] Standard three-point Gaussian interpolation was used to determine the (sub-pixel) location of correlation peaks[18] (Fig. 1c). Finally, a thin-plate spline approximation was used again to give the cor-

rected displacement field $\mathbf{du}^{**}$ (Fig. 2b). The incremental displacements $\mathbf{du}$ for $\mathcal{R}$ were then readily calculated by interpolation of the corrector function at each vertex location. The time to compute the full incremental displacement field for a pair of 3-megapixel images ($n_f = 8$; $\sim$2000 sub-windows) was on the order of 10 min using a 2.6 GHz Pentium 4 PC. Therefore, for a typical time-lapse sequence consisting of 100 frames, the total computational time was in the range of 15–17 h.

Calculation of Kinematic Quantities

The total Lagrangian or material displacement field for the region R at any time is given by the sum of the incremental displacements, $\mathbf{u}(t_n) = \sum_{i=1}^{n-1} \mathbf{du}(t_i)$. For notational convenience, we simply use $\mathbf{u}$ when the meaning is not otherwise unclear. In effect, once the time-varying displacement field is known, the trajectories for any arbitrary tissue material points can be determined, just as fluid streamlines determine the path of real or computationally-seeded flows.

The components of the deformation gradient $\mathbf{F}$ at any arbitrary location in $\mathcal{R}$ are given by $F_{ij} = \delta_{ij} + \tilde{u}_{i,j}$, where δ_{ij} is the kronecker delta, $\tilde{\mathbf{u}}$ is a continuous spline representation for $\mathbf{u}$, and $\tilde{u}_{i,j}$ represents partial differentiation ($i, j = x, y$). The symmetric Green–Lagrange strain tensor is given by $\mathbf{E} = \frac{1}{2}(\mathbf{F}^T\mathbf{F} - \mathbf{I})$, where $\mathbf{I}$ is the identity tensor. Note that $\mathbf{F}$ is a relative measure of deformation with respect
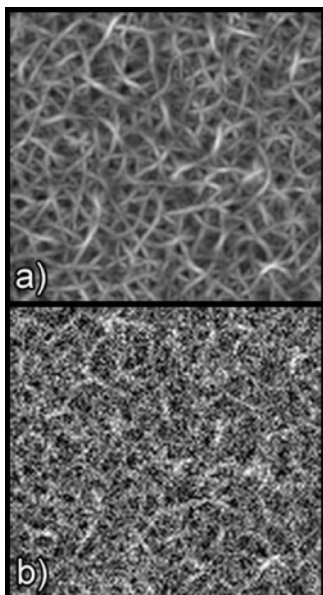
FIGURE 3. (a) Synthetic image created using ImageJ, as described in text, (b) Identical image corrupted with Gaussian noise ($\sigma = 40$).
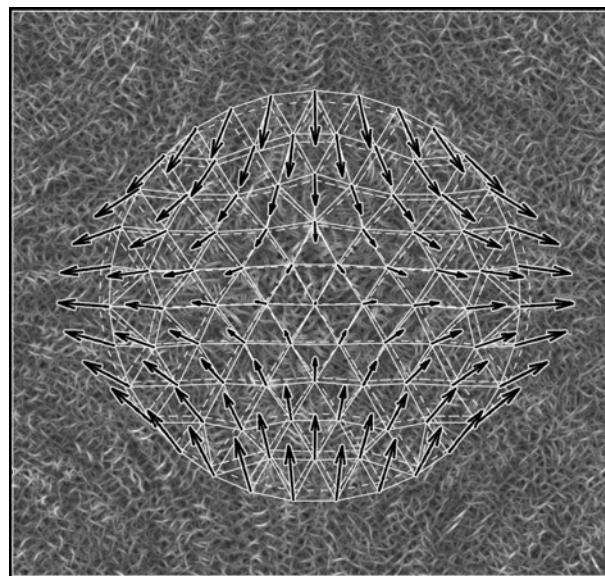

FIGURE 4. Displacement field calculated for PIV affine transformation (biaxial stretch) validation test. Shown here is a double image (base image + transformed image) with the original mesh (solid lines) and deformed mesh (dashed lines) found by the PIV algorithm. Arrows indicate direction and relative magnitude of displacement vectors for each vertex or material point.

to the initial configuration $\mathcal{R}$, which, as stated earlier, does not necessarily represent a true stress-free state.

Generation of Synthetic Motion Sequences for PIV Validation

Synthetic image motion sequences were created using ImageJ,[1] a freely-downloadable Java-based environment for image analysis. First, the pixels of a 512×512 image were assigned an 8-bit (0–255) grayscale intensity value from a purely random Gaussian distribution (i.e. white noise). This noisy image was then transformed into a synthetic texture pattern using a 4th-order steerable edge-detection filter,[11] which is available as a free Java plugin for ImageJ[2] (Fig. 3a). Although completely synthetic, the textures created in this way appear similar to very intricate isotropic fibril meshes that may be seen, for example, in electron micrographs of collagen gel networks. Rigid-body translations and rotations, as well as homogeneous affine-transformations (Fig. 4), were applied to a base image using another freely-available plugin filter called TransformJ.[3] TransformJ enables images to be spatially transformed using very accurate higher-order spline interpolation methods.[16] In some of the test sequences, additional Gaussian noise, specified by a standard deviation σ, was added to assess the behavior of the algorithm under more challenging conditions (Fig. 3b).

---

[1]http://rsb.info.nih.gov/ij.

[2]http://bigwww.epfl.ch/demo/steerable.

[3]http://www.imagescience.org/meijering/software/transformj.

RESULTS

Validation of PIV Algorithm

Standard PIV Tests Using Synthetic Motion Sequences

In general, the first and most fundamental criterion used to assess the validity of any digital PIV algorithm is the accuracy, in terms of absolute pixel error, in reproducing the displacement field for images translated, rotated, or deformed by a (usually homogeneous) known amount. Thus, the PIV algorithm should be able to measure rigid-body translations or rotations accurately without introducing significant non-zero strains. The algorithm should also be able to reproduce the uniform strain field prescribed by a simple affine transformation.

To address these issues, we first tested the proposed algorithm on synthetic images that were translated by either a whole-pixel or half-pixel in the *x*-coordinate direction. A uniform circular mesh with 90 vertices and a 175-pixel radius placed in the middle of the first image was used for measuring displacements. In both cases, the algorithm proved to be very accurate (Fig. 5a). Even for the whole-pixel translation sequence most heavily corrupted with noise ($\sigma = 40$), which gave the worst performance, the mean absolute pixel error was less than 0.03 pixels. The algorithm does not seem to exhibit significant integer peak-locking effects common to many PIV algorithms, which often have difficulties with the half-pixel test.[23] We

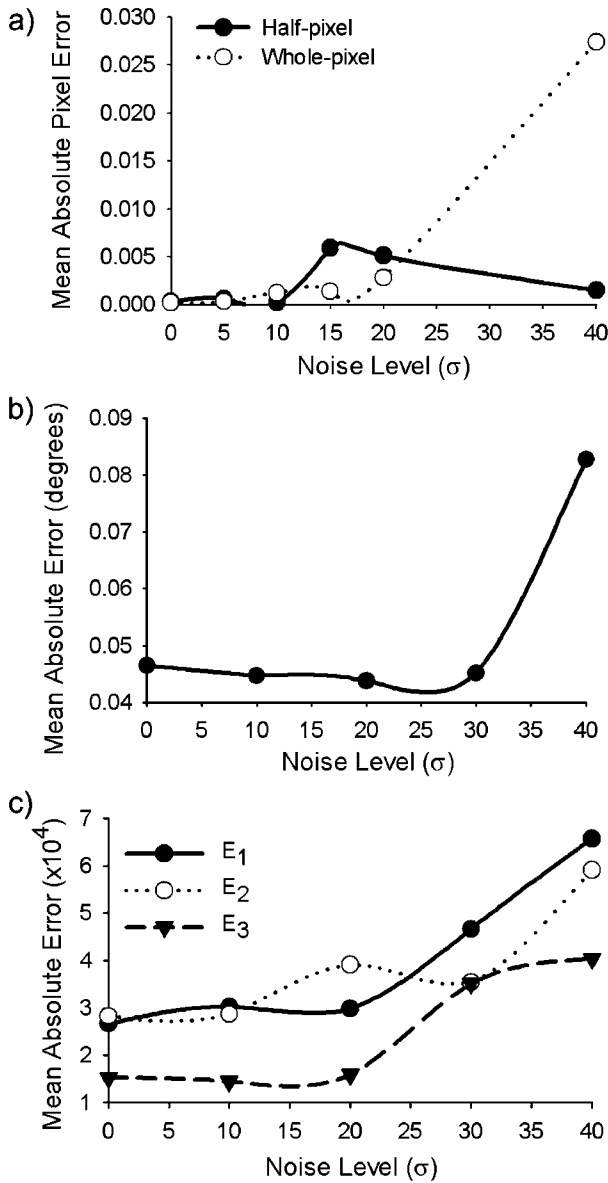**FIGURE 5.** The effect of increasing Gaussian noise with standard deviation σ was examined for some standard PIV validation tests: (a) half-pixel and whole-pixel rigid-body translation; (b) 5° clockwise rotation; and (c) affine transformation (biaxial stretch). In (c), E_1 and E_2 are the diagonal Green-Lagrange strain components, and E_3 is the (symmetric) off-diagonal or shear component. The mean absolute error in each case is with respect to the prescribed value, as given in the text.

speculate that the success of the algorithm in this respect may be due to the thin-plate spline interpolation that was used.

Second, we tested the ability of the algorithm to reproduce a relatively large rigid-body rotation, at least, in comparison to our experimental observations. In this case, the base image was rotated clockwise by 5°. As shown in Fig. 5b, the algorithm again performed consistently well in

this test, with mean absolute errors less than 0.05° in all but the worst-case. The Green–Lagrange strains produced by the rigid-body rotation test were negligible (data not shown).

Third, we prescribed a uniform 5% biaxial stretch, which gave the diagonal Green–Lagrange strains $E_{11} = 0.05$ and $E_{22} = -0.05$, and the off-diagonal strains equal to zero (Fig. 4). Although the mean absolute strain error clearly increased with added noise, once again, the error in each strain component was small (Fig. 5c), by any standards.

Finally, to simulate the effect of increasing frame rate, we compared the accuracy of the PIV method for several different amounts of incremental stretch (1, 2, 4, 5%) giving the same total strain over several steps (20%). To summarize the results, we found that there were no signifcant differences between the different tests, unless the absolute displacements being measured were greater than the interrogation window size $s + 2r$ (data not shown), which then resulted in some spurious solutions. In this case, the interrogation window was enlarged, thus restoring accuracy. For uniform affine tests, in general, increasing the interrogation window and/or sub-window does not cause a loss of accuracy; however, for real-world situations, increasing the size of the interrogation window may lead to decreased accuracy (due to noise), while increasing the size of the sub-window essentially decreases the spatial resolution. The specific experimental system must be designed (heuristically) to balance the desire for high spatial resolution with the requirement for maintaining measurement accuracy and precision.

Experimental Validation Test Using Cultured HUVEC Cells

The true measure of any PIV algorithm is generally borne out by experimental validation. To provide a challenging real-world experimental validation test for our algorithm, we cultured HUVEC cells (human umbilical vein endothelial cells) on a thick ($>100\,\mu$m) collagen gel (Type I rat tail collagen, 1 mg/mL, BD-Biosciences, Bedford, MA). Small, 6-μm diameter, polystyrene microspheres (Polysciences, Inc., Warrington, PA) were embedded in the gel, serving as passive markers for tissue deformation. The cells were then imaged using a 20X objective on an inverted microscope (Leica DMIRE2) for approximately 4 h at 3 m 30 s intervals. Although many cells were seen crawling, and several were observed undergoing mitosis, the microspheres exhibited little total displacement during the entire experiment, indicating that large-scale deformation of the gel was almost negligible (Fig. 6). In this experiment, the tissue material point trajectories calculated by the method more closely approximated those of the microspheres, rather than individual cells. This suggests the algorithm was able to
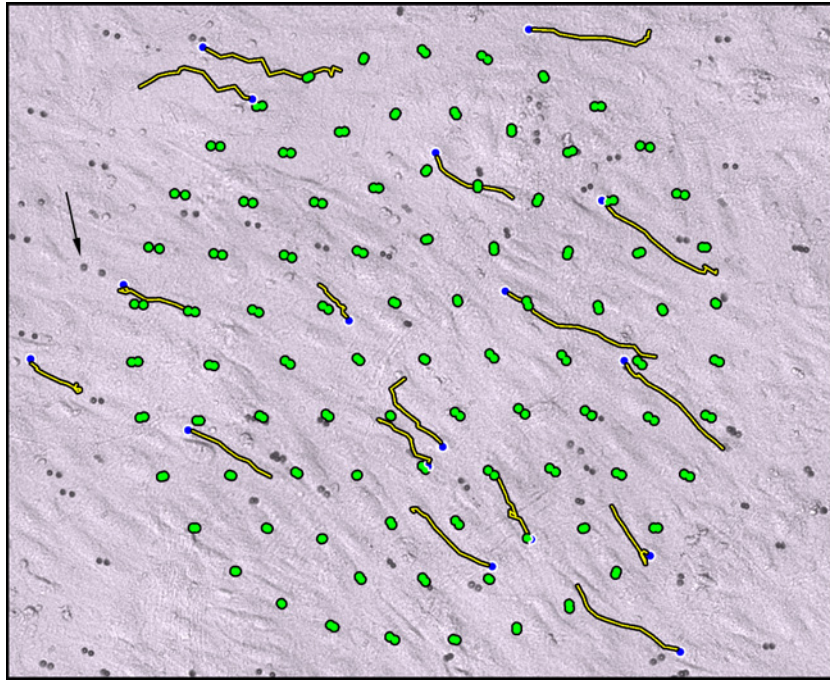
FIGURE 6. Double image of first and last frames for a time-lapse experiment showing cultured HUVEC cells on a collagen gel with embedded 6-μm polystyrene microspheres (black arrow). Trajectories for several cells that were tracked manually (small dot indicates end of each trajectory) indicate the extent of cell-level motion during the experiment. Nevertheless, displacements of virtual tissue material points (long dots) calculated by the proposed PIV algorithm more closely match those of the microspheres, rather than individual cells.

filter out local cell motion or motility that was not correlated at the (tissue-level) length-scale chosen for analysis.

Illustrative Data for Early Stage Quail Embryo

To illustrate the method, we first performed an imaging experiment on a normal HH7 (4-somite stage) quail embryo. At this stage of development, the embryo is essentially planar caudal to the developing foregut and omphalomesenteric veins near the heart. The embryo was microinjected in the lateral plate and caudal mesoderm with a fibrillin-2 fluorescent label (JB3 antibody), and allowed to pre-incubate for 1 h before the experiment, to allow for diffusion of the label. The embryo was then imaged under brightfield and fluorescent conditions for 10 h at 5 m 30 s intervals. We assume that the endoderm (ventral-most tissue germ layer) was mainly imaged in brightfield mode (Fig. 7a and b), because the embryo was positioned with the ventral surface facing the microscope objective. In addition, we assume the fibrillin-2 images, which were captured in the fluorescent mode, represent the mesoderm (middle tissue germ layer) (Fig. 7c and d).[19]

To obtain tissue fate and morphogenetic strain maps, a circular mesh $\mathcal{R}$ was placed symmetrically about the embryonic midline, encompassing all existing somites (at the beginning of the experiment) and the caudal portion of the notochord. The displacements and strains were then cal-

culated, as described in the Methods. It should be quite apparent that the PIV method can provide a tremendous amount of data, given that any set of arbitrary material points can be mapped for any period of time. For the purposes of this study, we chose to analyze a single region of the embryo that (1) always remained planar, as determined by visual inspection, and (2) contained sufficient image information or detail necessary for proper PIV analysis. It should be noted as an important experimental detail that the brightfield images inherently contain image information everywhere, but fluorescent images, such as fibrillin-2 used here, are mainly limited by their specific spatial labeling pattern. For example, fibrillin-2 labeling appears to be less intense and more sporadic near Hensen's node, which is the region caudal to $\mathcal{R}$ (Fig. 7c). Therefore, in general, the results in more sparsely labeled regions should be interpreted with relative caution, just as is the case for any PIV-type analysis.

There are several important phenomena to observe. What is most striking, perhaps, is that the overall pattern of motion or tissue deformation is so similar between the endoderm and mesoderm, as is shown by the tissue fate maps (Fig. 7) and strain maps (Fig. 8). There appear to be some subtle differences, however, especially at the anterior region, which may indicate some shearing or relative sliding between tissue layers near the omphalomesenteric veins. Second, the largest component of tissue displacement (and
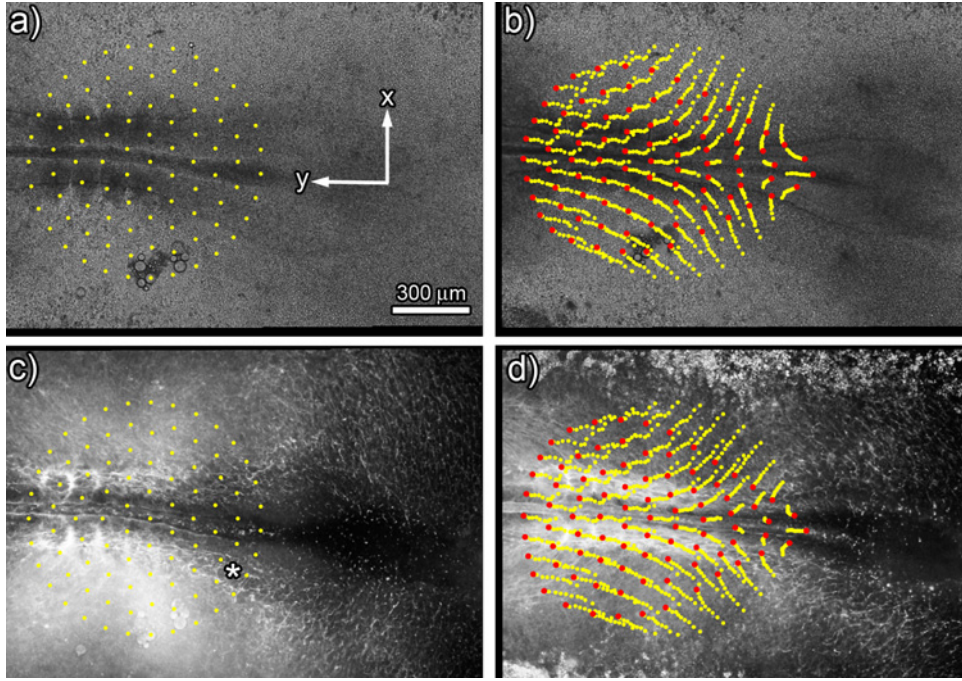
FIGURE 7. Tissue fate maps are shown for a 4-somite stage (HH7) quail embryo. Shown in (a) brightfield and (c) fluorescent (fibrillin-2) images are the initial configurations ($\mathcal{R}$) at the start of incubation. Tissue material points (yellow dots) to be analyzed were placed in an identical uniform circular pattern and trajectories were calculated as described in the text. The images in (b) and (d) show the embryo and trajectories after approximately 5 h of incubation. Here, one out of every six frames (approximately 30-min intervals) is represented by a yellow dot, and the red dots indicate the end of each trajectory.
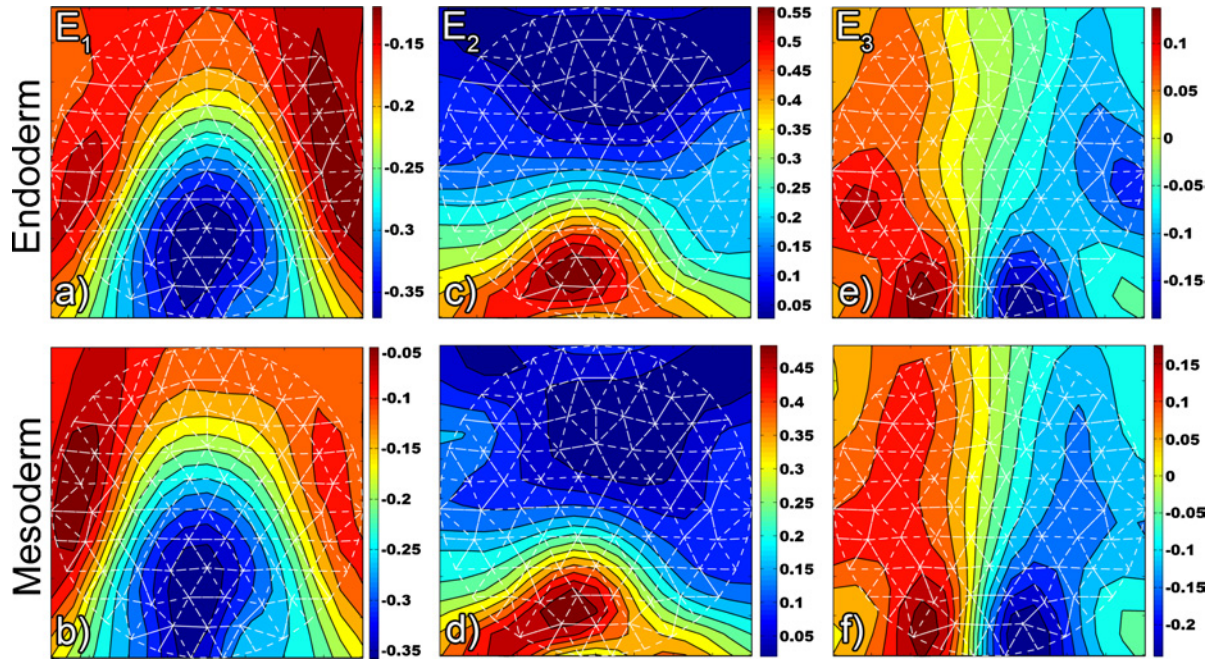

FIGURE 8. Total Green–Lagrange strains E for endoderm (a,c,e) and mesoderm (b,d,f) were calculated using brightfield and JB3-labeled fibrillin-2 time-lapse sequences, respectively, for the same embryo shown in Fig. 7, as described in the Methods. Here, $E_1 = E_{xx}$ (a,b) and $E_2 = E_{yy}$ (c,d) are the diagonal components of E, and $E_3 = E_{xy}$ (e, f) is the (symmetric) off-diagonal or shear component, with respect to the coordinate system defined in Fig. 7a. Strain contours are drawn with respect to the initial tissue configuration, which is represented by the overlaid circular mesh in each plot.
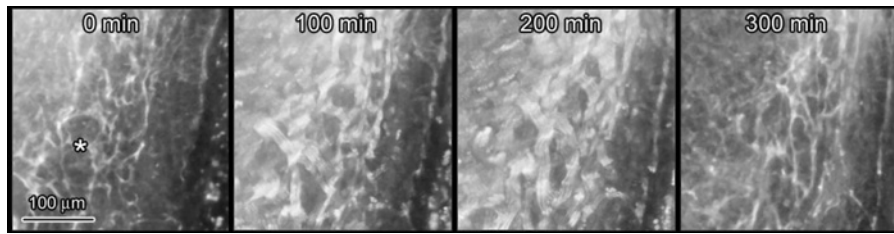
FIGURE 9. Closeup of embryo (corresponding asterisk in Fig. 7c) showing the fibrillin-2 network motion toward the axial midline. The middle two images are projections composed of several sequential images to emphasize the large-scale correlated motion produced by axial elongation of the embryo.

deformation) appears to be directed anteriorly and toward the axial midline. As a consequence, large-scale structures are pulled into close proximity with the somites. Lateral compression (Fig. 8a and b) and axial tension (Fig. 8c and d) are readily apparent in observing the deformation and remodeling of the fibrillin-2 network caudolateral to the last formed somite near the caudal end of the notochord (Fig. 9). Third, there exists a high degree of symmetry with respect to the embryonic axis, as perhaps, should be expected. In addition to direct comparison of the tissue fate maps on opposite lateral sides of the embyronic midline (Fig. 7b and d), almost perfect axial symmetry is seen in all three measures of strain (Fig. 8). Finally, it is important to note the cranial to caudal spatial strain gradients that arise, presumably due to the combined forces of notochord elongation and regression of Hensen's node. Although the total strain data shown in Fig. 8 is static with respect to the initial tissue configuration, the temporal evolution of strain fields in the embryo is suggested.

Next, we performed a time-lapse experiment on a different embryo, using only the brightfield illumination mode. Images were captured for several hours at 4-min intervals, beginning at the primitive streak stage (∼HH5). For this embryo, the undeformed mesh $\mathcal{R}$ was overlaid with the caudal end of the notochord near the center (Fig. 10a). The PIV analysis revealed large deformation of the endoderm, even during this relatively short period of development (Fig. 10b–d). In addition to demonstrating the ability of the method to capture large deformations *in vivo*, we would like to point out that these results also provide additional experimental validation for the ability of the method to provide smooth or continuous solutions, in the sense that neighboring material points always move together (i.e. mesh triangles never overlap or encroach upon their neighbors). The evolution of the total strain field for the tissue, with respect to the initial configuration, is shown in Fig. 11. It should be apparent from these strain data that the overall pattern of tissue deformation was relatively
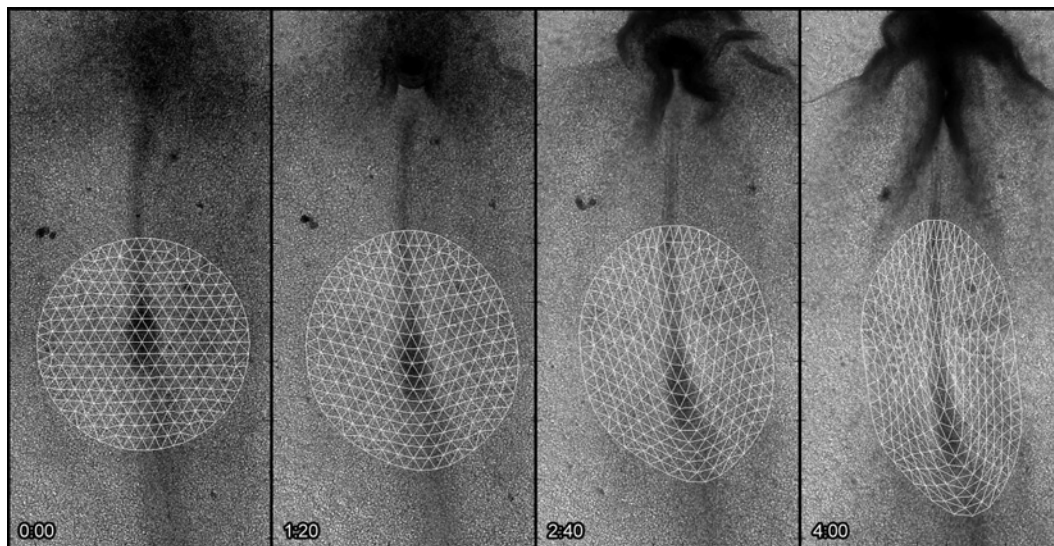

FIGURE 10. A quail embryo beginning at the primitive streak stage (∼HH5) is shown in brightfield for several time points (elapsed time in h:mm). Morphogenesis of the head-fold (cranial) and notochord elongation (caudal) occur simultaneously in the embryo during this period. Here, the time-varying tissue fate map, determined by the PIV algorithm, is drawn as a connected mesh to emphasize the tissue deformation.
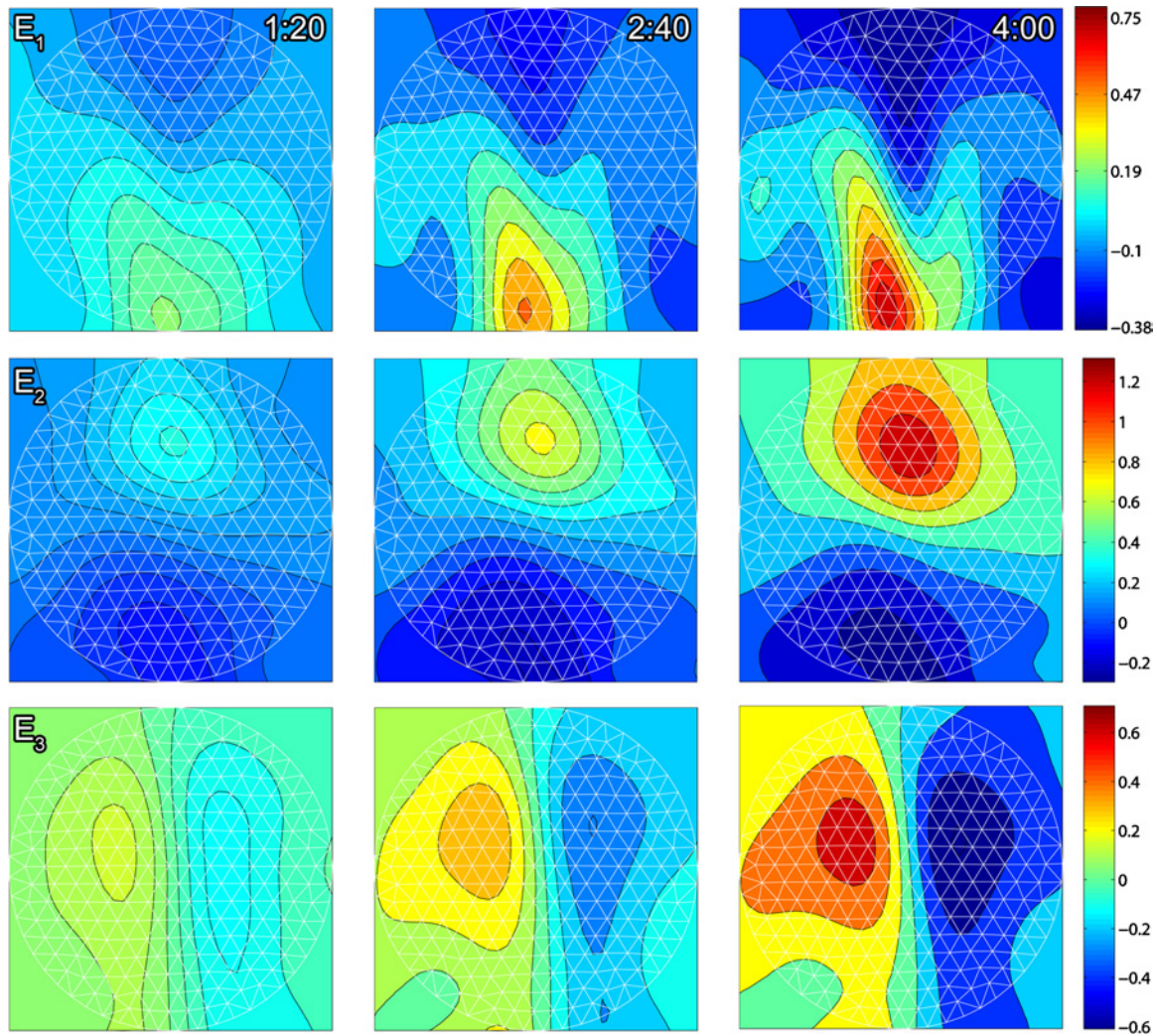
FIGURE 11. Green–Lagrange strain history for the embryo shown in Fig. 10. Each row corresponds to a particular component of the strain tensor E (according to the shorthand notation already given), and each column corresponds to the time point (h:mm) displayed in the top right corner of the top row. The numerical scale for each row is shown at the right side of the third column. All strain maps are drawn with respect to the initial tissue configuration (seen as overlaid mesh) in Fig. 10.

constant, although the magnitude of strains noticeably increased during the experiment.

DISCUSSION

In this study, we introduced and validated a method for computational tissue fate mapping in the early avian embryo, based on well-established digital PIV or image-based correlation techniques.[18,23] Tissue fate mapping, as opposed to classical cell fate mapping or other time-lapse cell tracking techniques, was used to track the displacements of virtual tissue material points in various layers of the embryo. Rather than relying on manual or semiautomatic (and possibly biased) tracking of microscopic structural features, such as the nuclei of individual cells[8] or the apparent intersections of ECM fbrils,[2] the method utilizes the tremendous amount of image information available in

the unique distribution of pixel intensities (in brightfield or fluorescent modes) to automatically determine the (incremental) displacement or deformation field giving the best correlation (i.e. maximum likelihood estimate) for an image pair. Here, we showed that in addition to enabling the measurement and visualization of trajectories for arbitrary material points in different imaging modes simultaneously (Fig. 7), the method provides the total (Lagrangian) displacement data necessary for calculating finite tissue strain maps (Fig. 8). These kinematic data will prove useful for characterizing large-scale morphogenetic movements and deformations, such as are seen in the fibrillin-2 ECM network (Figs. 7a,b and 9) or endodermal tissue layer (Figs. 7c,d and 10) during avian development. Moreover, tissue strain is likely to be directly related to the development of residual stresses in the embryo.[1] Mechanical testing methods in the embryo, such as microindentation,[26] will be

necessary to understand more fully this important feature of morphogenesis. Although not studied in this work, time-varying displacement data can also be used to calculate maps for the rate of tissue deformation.

Similar automated digital image correlation techniques have been used previously to study traction forces generated by fibroblasts[24] and the deformation of endothelial cells exposed to fluid shear forces.[10] In contrast to these *in vitro* cell-based studies, our method was conceived to behave essentially as a "low-pass" spatial deformation filter, thereby ignoring image information that is not well-correlated at the macroscopic or whole-embryo length-scale—local cell motility and migration being the most obvious examples (see Fig. 6). The main idea we want to emphasize here is that the length-scale of the analysis can be chosen *a priori* to facilitate or enable a true multi-scale experimental approach. For example, our results suggest that cell motility in the embryo could be determined more rigorously by tracking and measuring the displacements of individual cells (using existing methods), and then subtracting the macroscopic tissue displacement determined by the PIV method. As both imaging and computational power rapidly increase, it is reasonable to assume it will soon be possible to perform such analysis in real time. This ability will allow large-scale tissue motions and very high-resolution cell-level details (such as protrusive activity) to be captured simultaneously in the same experiment; for example, by using multiple objectives with different magnifying power, or, perhaps, combining widefield epifluorescence with confocal or two-photon capabilities.

The main limitations of the method are technical. Currently, there is no practical way to obtain high spatial and temporal resolution simultaneously in all three dimensions at macroscopic length scales in the embryo. For relatively thin planar tissues, such as examined in this study, the current 2-D method is appropriate, and interpretation of the quantitative results is unambiguous. For more three-dimensional structures, such as the heart or neural tube, the 2-D tissue fate map approximates or resembles a projection of the true 3-D solution. Nevertheless, even in these situations, the method may provide a useful starting-point for more quantitative study. If it were possible to obtain true high-resolution 3-D image data, and we expect this will occur in the not-too-distant future, *n*-dimensional generalization of the correlation method is straightforward, if not trivial. The most obvious biological factor limiting the method is the availability of appropriate cell and tissue markers. Needless to say, there is currently a tremendous amount of interest in finding fluorescent labels that are both specific and robust for imaging purposes (i.e. stable and bright). We are certainly not alone in this endeavor.

It is increasingly clear that the study of vertebrate morphogenesis, and development, in general, will benefit from quantitative biomechanical analysis at several length-scales, ranging from the tissue or organ level to the sub-cellular level. There are currently few data, however, concerning the general behavior of embryonic tissues at length-scales much greater than a single cell. The phenomenon of convergent extension, which is hypothesized to be fundamentally involved in several developmental processes (e.g. notochord and neural tube formation), has been widely studied in recent years,[4,8,13,14] but the main focus of these studies was cell-level motility. In this study, we presented new representative tissue fate and strain mapping data for the warm-blooded avian embryo. Although these results were primarily intended to be illustrative of the method, we would like to propose that these types of image-based correlation data are inherently robust, due to the voluminous amounts of information contained in the 4-D image data sets, even for a single embryo. Future studies will be necessary for providing measures of statistical significance.

These quantitative data demonstrate large tissue-level morphogenetic deformations occuring in the vertebrate embryo (Figs. 10 and 11). We showed for the first time, to our knowledge, that large-scale patterning of tissue motion may be very similar between different tissue layers, such as the mesoderm and endoderm (Figs. 7 and 8), suggesting the presence of global or whole-embryo mechanical processes. Moreover, the data presented here strongly suggest that it is precisely at the longer (i.e. millimeter) length scales that much of embryonic morphogenesis may be coordinated or regulated. It is now well known that mechanical forces can regulate cell behavior *in vitro*, but there remains much to be learned about the effects of mechanical stress on cells *in vivo*, and in the embryo, specifically. We believe that newer multi-scale experimental methods and computational biomechanical models will become essential, if not necessary, tools for improving our understanding of the complex interplay between cell-level activities and large-scale or tissue-level morphogenetic processes that shape the vertebrate embryo.

ACKNOWLEDGMENTS

REFERENCES

[1]Beloussov, L., J. Dorfman, and V. Cherdantzev. Mechanical stresses and morphological patterns in amphibian embryos. *J. Embryol. Exp. Morphol.* 34(3):559–574, 1975.
[2]Czirók, A., B. Rongish, and C. Little. Extracellular matrix dynamics during vertebrate axis formation. *Dev. Biol.* 268:111–122, 2004.

[3]Czirók, A., P. Rupp, B. R.ongish, and C. Little. Multi-field 3D scanning light microscopy of early embryogenesis. *J. Microsc.* 206:209–217, 2002.

[4]Elul, T., M. Koehl, and R. Keller. Cellular mechanism underlying neural convergent extension in *Xenopus laevis* embryos. *Dev. Biol.* 191(2):243–258, 1997.

[5]Filla, M. B., A. Czirók, E. A. Zamir, C. D. Little, T. J. Cheuvront, and B. J. Rongish. Dynamic imaging of cell, extracellular matrix, and tissue movements during avian vertebral axis patterning. *Birth Defects Res Part C Embryo Today* 72(3):267–276, 2004.

[6]Eraser, S., and R. Harland. The molecular metamorphosis of experimental embryology. *Cell* 100:41–55, 2000.

[7]Gilbert, S. Developmental Biology, 7th ed., Sunderland, MA: Sinauer Associates, 2003.

[8]Glickman, N. S., C. B. Kimmel, M. A. Jones, and R. J. Adams. Shaping the zebrafish notochord. *Development* 130(5):873–887, 2003.

[9]Hamburger, V., and H. Hamilton. A Series of Normal Stages in the Development of the Chick Embryo. *J. Morphol.* 88:49–92, 1951.

[10]Helmke, B., A. Rosen, and P. Davies. Mapping mechanical strain of an endogenous ctyoskeletal network in living endothelial cells. *Biophys. J.* 84:2691–2699, 2003.

[11]Jacob, M., and M. Unser. Design of Steerable Filters for Feature Detection Using Canny-Like Criteria. *IEEE Transactions on Pattern Analysis and Machine Intelligence* 26(8):1007–1019, 2004.

[12]Keller, R., L. Davidson, and D. Shook. How we are shaped: The biomechanics of gastrulation. *Differentiation* 71:171–205, 2003.

[13]Keller, R. Shaping the vertebrate body plan by polarized embryonic cell movements. *Science* 298(5600):1950–1954, 2002.

[14]Keller, R., L. Davidson, A. Edlund, T. Elul, M. Ezin, D. Shook, and P. Skoglund. Mechanisms of convergence and extension by cell intercalation. *Philos Trans R Soc Lond B Biol Sci* 355(1399):897–922, 2000.

[15]Little, C., and C. Drake. Whole-mount immunolabeling of embryos by microinjection. *Meth. Mol. Biol.* 135:183–189, 2000.

[16]Meijering, E., J. Wiro, and M. Viergever. quantitative evaluation of convolution-based methods for medical image interpolation. *Med. Image Anal.* 5:111–126, 2001.

[17]Persson, P., and G. Strang. A simple mesh generator in MAT-LAB. *SIAM Rev.* 46:329–345, 2004.

[18]Raffel, M., C. Willert, and J. Kompenhans. Particle Image Velocimetry, Berlin: Springer-Verlag, 1998.

[19]Rongish, B., C. Drake, W. Argraves, and C. Little. Identification of the developmental marker, JB3-Antigen, as Fibrillin-2 and its de novo organization into embryonic microfibrous arrays. *Dev. Dyn.* 212:461–471, 1998.

[20]Rupp, P., A. Czirók, and C. Little. $\alpha_v \beta_3$ integrin-dependent endothelial cell dynamics in vivo. *Development* 131:2887–2897, 2004.

[21]Rupp, P., A. Czirók, and C. Little. Novel approaches for the study of vascular assembly and morphogenesis in avian embryos. *Trends Cardiovasc. Med.* 13:283–288, 2003a.

[22]Rupp, P., B. Rongish, A. Czirók, and C. Little. Culturing of avian embryos for time-lapse imaging. *Biotechniques* 34:274–278, 2003b.

[23]Scarano, F. Iterative image deformation methods in PIV. *Meas. Sci. Technol.* 13:1–19, 2002.

[24]Vanni, S., C. Lagerholm, C. Otey, D. Taylor, and F. Lanni. Internet-based image analysis quantifies contractile behavior of individual fibroblasts inside model tissue. *Biophys. J.* 84:2715–2727, 2003.

[25]Wang, C., J. Deng, G. Ateshian, and C. Hung. An automated approach for direct measurement of two-dimensional strain distributions within articular cartilage under unconfined compression. *J. Biomech. Eng.* 5:557–567, 2002.

[26]Zamir, E. A., and L. A. Taber. On the effects of residual stress in microindentation tests of soft tissue structures. *J. Biomech. Eng.* 126(2):276–283, 2004.